RSC Mechanochemistry

ROYAL SOCIETY OF CHEMISTRY

PAPER

View Article Online
View Journal

Open Access Article. Published on 28 August 2025. Downloaded on 10/9/2025 2:34:38 PM.
This article is licensed under a Creative Commons Attribution-NonCommercial 3.0 Unported Licence.

Check for updates

Cite this: DOI: 10.1039/d5mr00062a

Structure–performance relationships of mechanochemically synthesized piezoelectric catalysts $BaTiO_3$, $NaNbO_3$ and $BiFeO_3$

Erin V. Phillips, [a] Van Son Nguyen, [b] Marta Hatzell [bc] and Carsten Sievers *[ac]

Piezoelectric catalysts were synthesized mechanochemically by converting $BaCO_3$ and TiO_2 to $BaTiO_3$, Na_2CO_3 and Nb_2O_5 to $NaNbO_3$ and Bi_2O_3 and Fe_2O_3 to $BiFeO_3$. The catalytic reactivity of $BaTiO_3$, $NaNbO_3$ and $BiFeO_3$ was tested using a mechanocatalytic arylation reaction involving 4-nitrobenzenediazonium tetrafluoroborate. The observed activity in the arylation reaction showed a dependence on the abundance of piezoelectrically active anisotropic phases as measured by the pre-edge intensity in XANES spectra of $BaTiO_3$ and $NaNbO_3$ and distribution of crystalline phases as measured by XRD for $BiFeO_3$. A kinetic analysis showed that the reaction over $BaTiO_3$ was limited by the amount of diazonium salt remaining in the reaction vessel, while the reaction over $NaNbO_3$ and $BiFeO_3$ was limited by the generation of electron hole pairs within the piezoelectric structure. This work shows that mechanochemically produced piezocatalysts have superior structural characteristics such as greater relative abundance of anisotropic phases, higher surface areas and smaller particle sizes that led the mechanochemically produced catalysts to outperform piezoelectric commercial counterparts when tested under the same arylation milling conditions.

Received 6th May 2025
Accepted 28th August 2025

DOI: 10.1039/d5mr00062a

rsc.li/RSCMechanochem

1. Introduction

Mechanochemistry is an emerging approach to chemical processes that utilizes mechanical forces in a ball mill, extruder or similar device to drive reactions in a milling environment.[1–3] Typically, either impact or shear forces are applied, resulting in continuous mixing and shearing within the reaction vessel. The potential applications for mechanochemistry span a wide variation of reactions from catalytic synthesis,[4–6] depolymerization and decomposition reactions,[7–10] to organic redox reactions.[11,12] The phenomena driving mechanochemical processes depend on the physical and chemical properties of the feedstock and can include a combination of creation of hot spots upon impact between the vessel wall and the mobile milling balls, the creation of transient catalytic sites, and increased solid–solid contact between the catalyst and feedstock mixtures.[1,13,14] In the spirit of green chemistry practices, mechanochemistry offers a promising approach for solvent-free reactions under nominally ambient conditions without the need for external heating or pressure.[1,14,15]

The electrical charge transfer that occurs through contact between two materials is known as a triboelectric effect, which has been observed in mechanochemical processes, wherein an electronic charge separation occurs upon mechanical impact.[1,16,17] Piezoelectric materials have the ability to form separated charges when a mechanical force is applied because of the polarizability of the piezoelectric unit cell.[17–20] Inherent material properties such as the piezoelectric charge coefficient (d), mechanical stress (σ) and the dielectric constant or permittivity (ε) govern the strength of the generated piezoelectric field, E.[21,22] A compressed piezo crystal can act as a redox catalyst.[16,17,20] For this reason, a mechanochemical environment was chosen for this study, in which ball milling provides direct and repeated impacts to piezoelectric catalysts. Specifically, this work studied the mechanochemical synthesis and reactivity of $BaTiO_3$, $NaNbO_3$, and $BiFeO_3$.

The properties of these materials can be understood in terms of multiferroic behavior, depending on the type of magnetoelectric effect that is inherently characteristic of the crystal structure. The simultaneous occurrence of ferroelectricity, ferromagnetism and/or ferroelasticity is referred to as multiferroic behavior and is generated from the inherent distortion of the piezoelectric unit cell. Piezoelectrically active phases include $BaTiO_3$ in tetragonal distortion,[23–26] $BiFeO_3$ in a rhombohedral distortion[27–30] and $NaNbO_3$ in an orthorhombic distortion.[31,32] Having an anisotropic unit cell is a defining characteristic of these structures. Upon application of stress or mechanical impact, the atoms are displaced from their original position, resulting in an overall net electrical charge. Thus, the distortion and elongation of the piezoelectric unit cell creates

[a]School of Chemistry and Biochemistry, Georgia Institute of Technology, Atlanta, GA 30332, USA. E-mail: carsten.sievers@chbe.gatech.edu

[b]School of Chemical & Biomolecular Engineering, Georgia Institute of Technology, Atlanta, GA 30332, USA

[c]George W. Woodruff School of Mechanical Engineering, Atlanta, GA 30318, USA

© 2025 The Author(s). Published by the Royal Society of Chemistry

Open Access Article. Published on 28 August 2025. Downloaded on 10/9/2025 2:34:38 PM.
This article is licensed under a Creative Commons Attribution-NonCommercial 3.0 Unported Licence.

an electric dipole within the structure. Greater abundance of the desired anisotropic piezoelectric lattice allows for easier electron transfer throughout the structure, as mechanical impact is converted to electrical potential.

However, these asymmetrical distortions are not permanent to the piezoelectric materials and can be altered to a non-active centrosymmetric phase with extended impact in a milling environment. Once the unit cell is centrosymmetric, the cell is no longer polarizable, and the piezo-catalyst is therefore deactivated because it cannot initiate an electron transfer. Depending on the catalyst, a cubic phase can be adopted from milling in the form of a lattice shift, atomic reorganization, or the formation of an entirely new phase. For $BaTiO_3$, the most common form of deactivation is a shift from tetragonal P_{4mm} to cubic P_{m3m},[24,33–38] where the unit cell remains intact, but the length of the *c*-axis is shortened, and the distortion of the material is lost. For $BiFeO_3$, $Bi_2Fe_4O_9$ and $Bi_{25}FeO_{39}$ (ref. 39–43) are the result of destruction of $BiFeO_3$ and are entirely new structures, which do not present the same strength of piezoelectrical properties, due to increased symmetry. Alternatively, $NaNbO_3$ shifts between different configurations with P_{bcm}, P_{mc21}, C_{cmm} and P_{mmn} space groups.[32,44,45] Many studies have previously examined the synthesis and behavior of piezoelectric materials in a mechanochemical environment with extended milling times. Most techniques utilize planetary mills with zirconia,[24,31,33,34,36,44–50] agate[35,51] or stainless-steel[38,39,42,43,52–54] vessels and milling times up to 30 days. This work, by contrast, examines synthesis using a vibratory mill with a tungsten carbide vessel. Planetary milling typically delivers greater shear forces, whereas vibratory milling offers greater direct impact forces. Many of the articles preceding this work used longer milling times to avoid additional heating.[35,41,44,48,52,55–57]

Kubota *et al.*[12] first demonstrated the activity of $BaTiO_3$ for mechanoredox arylation and borylation reactions in 2019 using a variety of aryl diazonium salt precursors. TEMPO (2,2,6,6-tetramethylpiperidinoxyl) was also used in this study as a radical scavenger to obtain more complex intermediate products with moderate success. Schumacher *et al.*[58] followed in 2020 with a copper-catalyzed transfer radical cyclization (ATRC) reaction using $BaTiO_3$. Monobromoacetamide was chosen as the alkyl halide, and solid tris(2-pyridylmethyl)amine (TPMA) was chosen as the ligand for the ATRC reaction, while copper triflate, $Cu(OTF)_2$, was the chosen salt; $BaTiO_3$ facilitated the reduction of Cu^{II}, which allowed it to be catalytically active for ATRC. Effaty *et al.*[59] and Wang *et al.*[60] followed in 2021 with a multitude of similar basic organic reactions, wherein two substrates were combined to form a singular product in the presence of $BaTiO_3$. In 2022, Wang *et al.*[61] explored the aerobic oxidative coupling of thiols, reaching yields exceeding 99%. In all of these studies, only commercial $BaTiO_3$ was used, and the material-specific properties of the mechanocatalysts were beyond the scope of these studies. On the other hand, piezoelectric materials, such as $NaNbO_3$ and $BiFeO_3$, have been synthesized *via* milling,[32,39,40,42–44,48–51,57,62] but their mechanocatalytic reactivity has not been investigated. In this paper, we report on mechanochemically synthesized piezoelectric materials used in mechanocatalytic reactions, where the synthesized materials exhibited superior performance due to greater surface area, smaller particle sizes, and a higher abundance of desired active phases when compared to commercial catalysts of the same configuration.

2. Materials and methods

2.1 Catalyst characterization

2.1.1 Materials. $BaCO_3$ (99.8%, 1 μm powder) was purchased from Alfa Aesar. Commercial $BaTiO_3$, and furan were obtained from Sigma Aldrich. Na_2CO_3 (99.5%) was purchased from STREM Chemicals. Nb_2O_5 (99.5%, ~150 μm powder) Bi_2O_3 (99%) and 4-nitrobenzenediazonium tetrafluoroborate (97%) were obtained from Thermo Scientific. Bulk TiO_2 (99.9%) and Fe_2O_3 (99.9%) were purchased from Fisher Scientific. Commerical $NaNbO_3$ (99.9%) was obtained from AA Blocks, while the 2-(4-nitrophenyl) furan standard was purchased from ChemScene (98.0%). Methanol (99.8%) (ACS grade) was purchased from VWR.

2.1.2 X-ray diffraction (XRD). XRD was performed using a Rigaku Miniflex Powder XRD system. A CuKα X-ray source was used at a wavelength of $\lambda = 1.54$ Å. A current of 40 mV was applied while the generator operated at a voltage of 15 kV. The spectra were measured from $2\theta = 20°$ to 90° with a step size of 0.01° and a scan speed of 10° per minute. Data analysis and Rietveld refinement was conducted using the HighScore Plus program.

2.1.3 X-ray absorption spectroscopy (XAS). X-ray absorption spectroscopy data was collected at Inner Shell Spectroscopy beamline (ISS, 8-ID) of the National Synchrotron Light Source (NSLS II) at the Brookhaven National Laboratory. The samples were pressed into wafers by diluting the catalysts with polyethylene glycol in a 1 : 10 ratio. Passivated Implanted Planar Silicon (PIPS) detector was used to collect fluorescence data. The energy was calibrated using Ti, Nb and Fe foils, measured together with the samples. The edge values were set to 4980 eV (Ti K-edge) for $BaTiO_3$ samples, 19 000 eV (Nb K-edge) for $NaNbO_3$ samples and 7125 eV (Fe K-edge) for $BiFeO_3$ samples. To process the data, the Demeter package was used.[63] Between 6 to 9 scans were collected and averaged for each sample to improve data quality.

2.1.4 N_2 physisorption. Surface area, pore volume, and pore diameter were measured using N_2 physisorption coupled with Brunauer–Emmett–Teller (BET)[64] multi-point measurement analysis. The analysis was conducted on a Micromeritics ASAP 2020 Accelerated Surface Area and Porosimetry System. Approximately 0.200 g of each sample was used during the analysis process. The sample was degassed to 10 mmHg and held under vacuum for 120 min before backfilling occurred and the sample was shifted to the analysis port where a standard N_2 physisorption method was used to complete the desorption.

2.1.5 Transmission electron microscopy (TEM). A FEI Tecnai F30 was used to obtain TEM images operating 300 kV. The instrument was equipped with a thermally assisted field emission (TFE) gun, and all images were converted and analyzed using a Gatan GIF system (Tridiem 863 UHS). A CompuStage single-tilt holder was used to hold the samples,

 © 2025 The Author(s). Published by the Royal Society of Chemistry

Open Access Article. Published on 28 August 2025. Downloaded on 10/9/2025 2:34:38 PM. This article is licensed under a Creative Commons Attribution-NonCommercial 3.0 Unported Licence.

and all images are shown on a scale of 20–200 nm. For preparation, approximately 5 mg of the samples were sonicated in 1 mL of ethanol and dispersed onto a holey carbon–copper 200 mesh grid.

2.1.6 Scanning electron microscopy (SEM). SEM was conducted using a Thermo Axia Variable Pressure Model with a thermionic tungsten filament source. The samples were prepared on carbon tape and were analyzed under high vacuum at 10.00 kV at a working distance of 9.0 to 9.6 mm. An Everhart–Thornley detector was used for SEM imaging, which ranged from 10 μm to 100 μm scales.

2.2 Synthesis and arylation milling conditions and product characterization

2.2.1 Milling procedures

2.2.1.1 Mixed metal oxide synthesis. To synthesize the piezoelectric catalysts $BaTiO_3$, $NaNbO_3$ and $BiFeO_3$, oxide and carbonate precursors were used, following the reactions:

$$BaCO_3 + TiO_2 \rightarrow BaTiO_3 + CO_2 \quad \text{(EQ1)}$$

$$Na_2CO_3 + Nb_2O_5 \rightarrow 2NaNbO_3 + CO_2 \quad \text{(EQ2)}$$

$$Bi_2O_3 + Fe_2O_3 \rightarrow 2BiFeO_3 \quad \text{(EQ3)}$$

All reactions were conducted using a Retsch MM400 vibrational ball mill with a 25 mL tungsten carbide (WC) milling vessel and 2 × 15 mm WC balls. The precursors were added in equimolar amounts in order to obtain 2 g of the final piezoelectric catalyst. Milling was conducted at 30 Hz from 0.5 to 5 h. Calcination was conducted for $BaTiO_3$ at a ramp of 10 °C per minute for 80 min up to 800 °C and held for 45 minutes before cooling. $NaNbO_3$ and $BiFeO_3$ were also heated at 10 °C per min up to 650 °C and held for 2 h before cooling. To differentiate between the synthesized *versus* commercial catalysts, catalysts made *via* milling are denoted as "HM" for "house-made", followed by milling time (0.5, 1, 2, or 5 h) and "C" to indicate that calcination was completed.

2.2.1.2 Arylation reaction. The arylation reaction utilized 4-nitrobenzenediazonium tetrafluoroborate and furan. The amounts used were approximately 0.30 mmol of salt to 4.5 mmol of furan and 1.5 mmol of catalyst; due to the volatility of furan at 31 °C, a significant excess was necessary. The reaction was carried out using a 25 mL stainless steel vessel and a single 20 mm stainless steel ball at 30 Hz for 1 h, followed by 30 min of cooling before the vessel was opened to collect the product mixture.

2.2.2 High permeation liquid chromatography (HPLC). During the collection of the product mixture, the contents were dissolved in a 50 mL mixture of methanol and water at a ratio of 85 : 15. An Agilent 1260 Infinity HPLC was used for the analysis, equipped with an Agilent Eclipse Plus C18 column. The injected amount was 3 μL at a draw and ejection speed of 200 μL min^{-1}. The flow rate was set at a constant 0.500 mL min^{-1} flow rate (85% MeOH to 15% H_2O), and the program time was set to 7 min. A UV-vis detector was used to analyze product concentration at wavelength of 242 nm.

2.2.3 Nuclear magnetic resonance (NMR). A Bruker AV3 400 MHz NMR spectrometer was used to analyze the purity of the crude product mixture and ensure that 2-(4-nitrophenyl) furan and 4,4′-dinitrobiphenyl were the only products detected. Product identification for 2-(4-nitrophenyl) furan was first conducted using NMR, followed by HPLC for quantitative analysis. Samples were prepared by measuring 75 mg of the crude mixture, which was dissolved in 1 mL of deuterated chloroform ($CDCl_3$). The samples were sonicated for 1 h, followed by centrifugation for 30 min to separate the catalyst from the dissolved products. The separated liquid was pipetted into an NMR tube and analyzed using ^1H NMR. For 1D proton spectra, Bruker standard zg30 pulse sequence was used with a pulse length of 13.25 μs and recycle delay time $d_1 = 1$ s. The pre-scan delay way set to 6.5 μs while number of scans was set to $n = 16$. The reference signal for $CDCl_3$ presented itself at 7.26 ppm.

2.2.4 Fourier transform IR spectroscopy with ATR attachment. The IR spectra for the diazonium salt pre- and post-reaction were measured using a Thermo Scientific™ Nicolet™ 8700 FTIR spectrometer with Smart iTR™ Attenuated Total Reflectance (ATR) accessory with a diamond internal reflection element (IRE). A few mg of the sample was placed over the IRE and was held in place using a clamp. The absorbance spectra were measured from 650 cm^{-1} to 4000 cm^{-1}. 64 scans were taken for each sample, while a fresh background was recorded before each set of sample scans.

3. Results

3.1 Crystalline phase and bulk composition analysis

$BaTiO_3$, $NaNbO_3$ and $BiFeO_3$ were synthesized by milling times ranging from 0.5 h to 5 h followed by calcination. Diffractograms for the catalysts before calcination can be found in Fig. S1, S3 and S6. After 0.5 h of milling, the diffractogram exhibited characteristic peaks at 22° (010), 32° (011), 38° (111), 45° (002), 51° (021), and 56° (112), confirming the presence of $BaTiO_3$ (Fig. 1A). Furthermore, there were no peaks corresponding to residual $BaCO_3$ or TiO_2. Rietveld refinement of the diffractogram was used to determine that the P_{4mm} phase and the P_{m3m} phase were the two main phases present. The peak at 45°, associated with the (002) crystal plane, displayed an intensity variation that suggested a transformation from the tetragonal (P_{4mm}) phase (lattice parameters: 3.99 Å, 3.99 Å, 4.02 Å)[24,33,34,36,38] to the cubic (P_{m3m}) phase (3.99 Å, 3.99 Å, 3.99 Å),[24,36,37] based on the increased peak intensity.[33,35,65,66] After 1 h of milling, the peak at 45° intensified further, indicating a continued phase transition from tetragonal to cubic symmetry. This trend was also observed in commercial $BaTiO_3$ (Fig. S1), which initially exhibited peaks corresponding to the tetragonal phase but gradually converted to the cubic phase with prolonged milling. Between 1 h and 5 h, peak broadening became evident, signifying increased disorder and amorphization. Rietveld refinement confirmed a growing fraction of the non-active cubic lattice (Fig. 1B), leading to a reduction in the material's piezoelectric potential. Since effective piezoelectricity requires an anisotropic lattice, the transition to a centrosymmetric cubic structure hindered charge separation and reduced

Open Access Article. Published on 28 August 2025. Downloaded on 10/9/2025 2:34:38 PM.
This article is licensed under a Creative Commons Attribution-NonCommercial 3.0 Unported Licence.

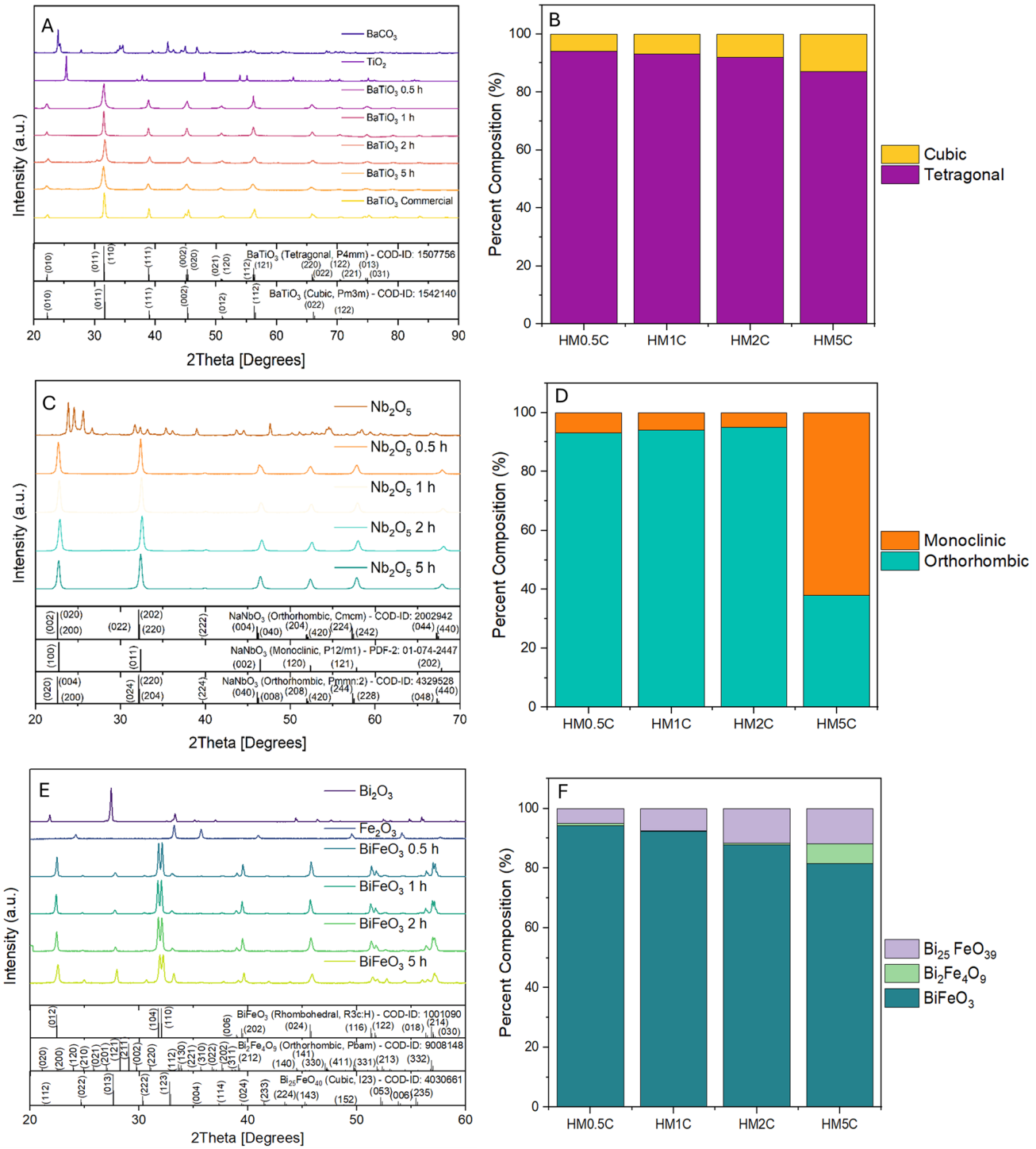

Fig. 1 (A) X-ray diffractogram of $BaCO_3$ and TiO_2 precursors and $BaTiO_3$ catalysts synthesized by 0.5–5 h of milling followed by calcination. Commercial $BaTiO_3$ is also shown as a reference. (B) Comparison in percent composition of $BaTiO_3$ between tetragonal and cubic crystal phases. (C) X-ray diffractogram of Nb_2O_5 precursor and $NaNbO_3$ synthesized catalysts from 0.5–5 h of milling followed by calcination. (D) Comparison in percent composition of $NaNbO_3$ between orthorhombic and monoclinic crystal phases. (E) X-ray diffractogram of Bi_2O_3 and Fe_2O_3 precursors and $BiFeO_3$ synthesized catalysts from 0.5–5 h of milling followed by calcination. (F) Abundance of $BiFeO_3$, $Bi_{25}FeO_{39}$ and $Bi_2Fe_4O_9$ for 0.5 h, 1 h, 2 h and 5 h of milling Bi_2O_3 and Fe_2O_3 after milling and calcination.

electron mobility. Consequently, prolonged milling time induces the transition in $BaTiO_3$ from a tetragonal to a cubic structure, eliminating its piezoelectricity due to structural centrosymmetry.

$NaNbO_3$ was synthesized from $NaCO_3$ and Nb_2O_5 in equimolar proportions and was found to follow a similar structural evolution to $BaTiO_3$. After 0.5 h of milling, diffractions corresponding to the precursors ($NaCO_3$ and Nb_2O_5) were no longer

 © 2025 The Author(s). Published by the Royal Society of Chemistry

Open Access Article. Published on 28 August 2025. Downloaded on 10/9/2025 2:34:38 PM.
This article is licensed under a Creative Commons Attribution-NonCommercial 3.0 Unported Licence.

detected (Fig. 1C), and new diffraction peaks emerged at 22.5° (002), 32.5° (202), 46.5° (004), 52.5° (204), and 58° (224), confirming the formation of $NaNbO_3$. Rietveld refinement of these peaks was used to determine that the C_{mcm} phase and the $P_{12/m1}$ phase were the two main phases present. The phase composition included both an orthorhombic C_{mcm} structure (lattice parameters: 7.83 Å, 7.84 Å, 7.85 Å) and a monoclinic $P_{12/m1}$ phase (3.91 Å, 3.91 Å, 3.91 Å).[31,32,44,48] The intensity ratio of the peaks at 32.5° and 22.5° allowed differentiation between these phases. In the C_{cmm} phase, the 32.5° peak was slightly more intense, whereas in $P_{12/m1}$, the 22.5° peak had a higher intensity. As milling progressed, an increasing fraction of the structure transformed from C_{cmm} to $P_{12/m1}$. Since $P_{12/m1}$ retains an angular distortion (one angle at 90.23°), it is piezoelectrically active, unlike the centrosymmetric cubic phase observed in $BaTiO_3$. Rietveld refinement showed that the relative fraction of $P_{12/m1}$ increased from 5–7% after 0.5 h to 62% after 5 h, with a corresponding decrease in C_{cmm} from 93–95% to 38% (Fig. 1D). Further milling induced the transformation of commercial $NaNbO_3$ into the $P_{mmn:2}$ phase (lattice parameters: 7.80 Å, 7.80 Å, 15.64 Å), characterized by equal peak intensities at 22.5° and 32.5°. This space group preserved its anisotropy and thus remained piezoelectric. Consequently, $NaNbO_3$ retained its piezoactivity over longer milling time due to the maintained anisotropic phases (C_{cmm} and $P_{12/m1}$), with $P_{12/m1}$ becoming more prevalent.

$BiFeO_3$ was synthesized from Bi_2O_3 and Fe_2O_3 under the same milling and calcination conditions as $NaNbO_3$. After 30 min, diffraction peaks at 22° (012), 31.9° (104), 32.2° (110), 39° (006), 39.5° (202), 46° (024), 51.5° (116), 52° (122), 56.5° (018), 57° (214), and 57.3° (030) confirmed the formation of $BiFeO_3$ through Rietveld refinement (Fig. 1E). The dominant lattice was $R_{3c:H}$ (lattice parameters: 5.58 Å, 5.58 Å, 6.39 Å), which is known for its antiferromagnetic properties.[57,62,67] Over longer milling time, two secondary phases emerged: the bismuth-rich $Bi_{25}FeO_{39}$ phase and the iron-rich $Bi_2Fe_4O_9$ phase. Minor peaks for $Bi_{25}FeO_{39}$ (I_{23} space group, lattice parameters: 10.15 Å, 10.15 Å, 10.15 Å) appeared after 30 min and increased with extended milling.[39–43,56,68,69]. $Bi_2Fe_4O_9$ (P_{bam}, lattice parameters: 7.62 Å, 8.11 Å, 5.85 Å) was initially undetectable but became prominent (>1%) after 5 h. Rietveld refinement confirmed a decreasing $BiFeO_3$ abundance, from 94.2% at 0.5 h to 81.5% at 5 h, while $Bi_{25}FeO_{39}$ increased from 5% to 12%, and $Bi_2Fe_4O_9$ rose from <1% to 6.5% (Fig. 1F). Although $BiFeO_3$ and $Bi_2Fe_4O_9$ retained their piezoelectric properties due to their non-centrosymmetric structures, the increasing fraction of $Bi_{25}FeO_{39}$, which is cubic and centrosymmetric, contributed to reduced piezoelectric activity. The decline in piezoelectric performance over time was correlated with the increasing presence of this inactive phase.

It is important to note that the abundance of phases in $BaTiO_3$, $NaNbO_3$ and $BiFeO_3$ based on Rietveld refinement is reported in relative terms but does not include contribution from possible amorphous phases or phases with concentrations below the detection limit. It is likely that there are other minor phases that form over time with extended milling impact, leading to slight variations in unit cell dimensions. For this reason, only phases with an abundance above 1% were reported. XRD references for $BaTiO_3$ (P_{4mm}, P_{m3m}), $NaNbO_3$ (C_{cmm}, $P_{12/m1}$, $P_{mmn:2}$) and $BiFeO_3$ ($R_{3c:H}$, I_{23}, P_{bam}) can be found in the SI (Fig. S2, S5 and S7).

In addition to XRD analysis, XAS was conducted to further understand transition states and oxidation states of the central Ti, Nb and Fe atoms, respectively. For $BaTiO_3$, the pre-edge feature at 4970 eV correlates to the excitation from the $Ti_{(1s)}$ to the $Ti_{(3d)}$ unoccupied state (Fig. 2A and B).[23,26,70,71] This excitation occurs in tandem with the dipolar transition of the $O_{(2p)}$ orbital to a hybridized $Ti_{(3d)}$ state.[30,72,73] This is indicative of ferroelectric off-centering, which is characteristic of strong piezoelectric properties.[23,26] A higher intensity of the pre-edge peak indicates a greater concentration of the anisotropic P_{4mm} phase, whereas centrosymmetric phases, such as P_{m3m}, do not give rise to this characteristic pre-edge peak. $BaTiO_3$ after 1 h of milling had the most intense pre-edge peak, indicating that this catalyst contained a greater abundance of the P_{4mm} lattice,[67] rather than the centrosymmetric P_{m3m} structure.[23] The commercial catalyst was the least active and contained the highest amount of P_{m3m} initially. No significant shift of the XANES edge was observed, and the oxidation state remained constant. Because $BaTiO_3$ was shown to be resistant to the formation of inactive phases and was solely subject to dimensional shifts, $BaTiO_3$ remained the only phase present. Moreover, Ti consistently maintained a +4 oxidation state.

The XAS spectra collected for $NaNbO_3$ (Fig. 2C and D) demonstrated a similar pattern as that in the spectrum of $BaTiO_3$. The spectrum is representative of the hybridization between the $Nb_{(4d)}$ state and the $O_{(2p)}$ state. The conduction band of $NaNbO_3$ is primarily composed of $Nb_{(4d)}$ orbitals while the valence band is mainly composed of $O_{(2p)}$ orbitals.[74] The hybridization between the conduction and valence band results in a covalent interaction, which is responsible for atom displacement in $NaNbO_3$.[75–77] The pre-edge peak present at 18 990 eV is therefore directly correlated to the presence of a greater relative abundance of the orthorhombic anisotropic phase of $NaNbO_3$. An additional shift of the pre-edge peak to even lower energies, as is observed from $NaNbO_3$ HM1C to HM2C, indicated atom displacement and increasing abundance of the desired $NaNbO_3$ phase.[75] Specifically, this shift is indicative of a more highly coordinated Nb–O environment.[75] The pre-edge peak for $NaNbO_3$ HM5C nearly aligned with HM1C, suggesting that a similar catalyst activity should be observed. In comparison to the commercial sample, which had the lowest intensity, one would expect to observe reduced catalytic activity. Similar to Ti in $BaTiO_3$, Nb maintained a +5 oxidation state, so the overall shifts of the XANES edge were minimal.

The XANES spectra of $BiFeO_3$ showed minimal changes of the oxidation state of iron with increasing milling time (Fig. 2E and F). With the Fe_2O_3 precursor, Fe remained as Fe^{3+} as $BiFeO_3$ was formed. The undesired phases $Bi_{25}FeO_{39}$ and $Bi_2Fe_4O_9$ also contained iron as Fe^{3+}. Therefore, no statistically significant shift was observed for the XANES edge position. The pre-edge peak, by contrast, increased in intensity as the realtive abundance of $Bi_{25}FeO_{39}$ and $Bi_2Fe_4O_9$ increased. Literature suggests

Open Access Article. Published on 28 August 2025. Downloaded on 10/9/2025 2:34:38 PM.
This article is licensed under a Creative Commons Attribution-NonCommercial 3.0 Unported Licence.

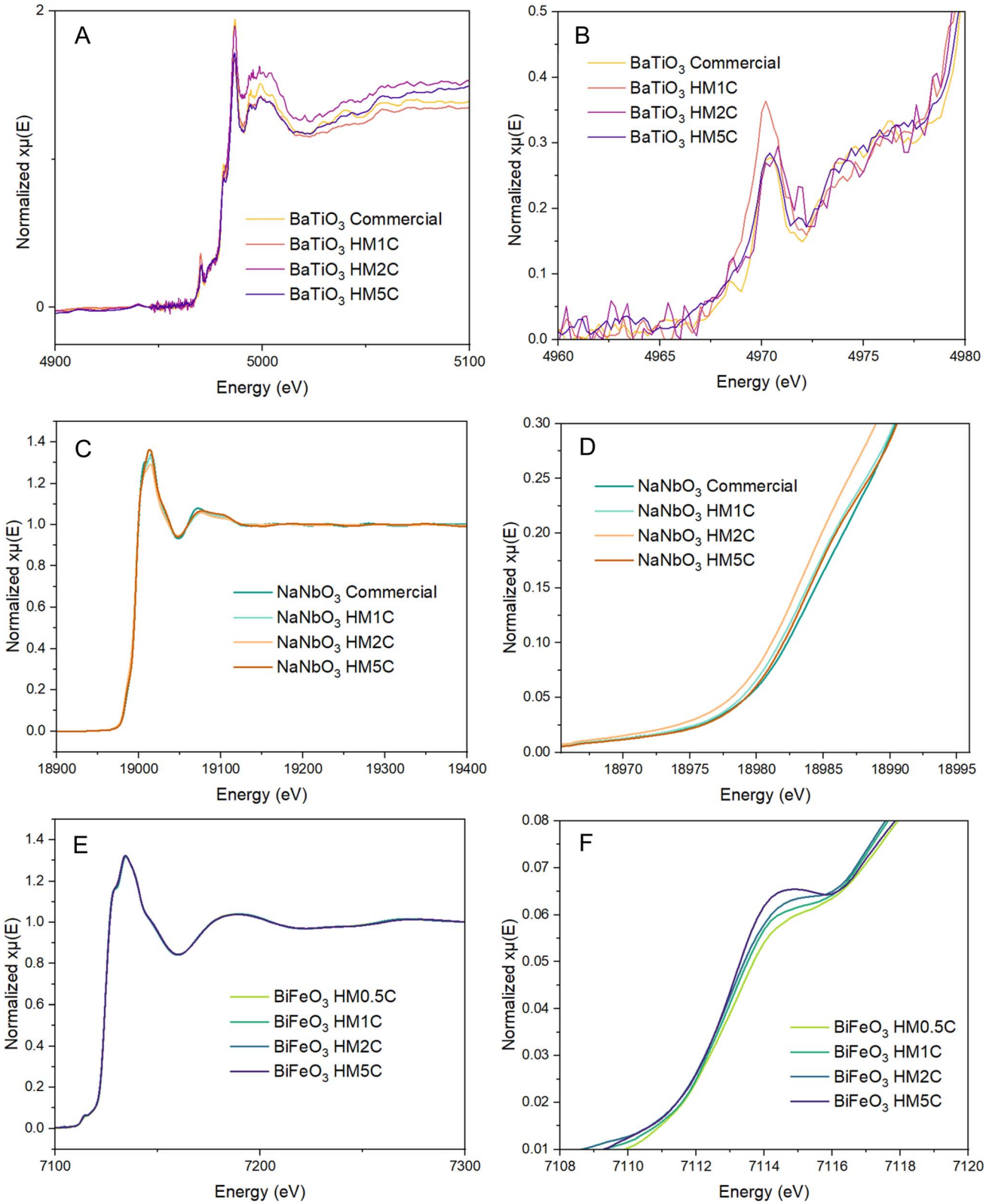

Fig. 2 XAS spectra at the Ti K-edge (A) for commercial $BaTiO_3$ and milled $BaTiO_3$ between 1–5 h. A close-up of the pre-edge peak at 4970 eV is shown on the right (B). XAS spectra at the Nb-K-edge (C) for the commercial and mechanochemically synthesized $NaNbO_3$ between 1–5 h. A close-up of the pre-edge peak at 18 990 eV is shown on the right (D). XAS spectra at the Fe-K-edge (E) for mechanochemically synthesized $BiFeO_3$ between 0.5–5 h. A close-up of the pre-edge peak at 7114 eV is shown on the right (F).

 © 2025 The Author(s). Published by the Royal Society of Chemistry

Open Access Article. Published on 28 August 2025. Downloaded on 10/9/2025 2:34:38 PM.
This article is licensed under a Creative Commons Attribution-NonCommercial 3.0 Unported Licence.

that the pre-edge peak for $BiFeO_3$ is indicative of the electric quadrupole-forbidden transition from the $O_{(1s)}$ level to the $Fe_{(3d)}$ level as hybridization occurs.[28,29,78,79] A higher pre-edge intensity correlates to a stronger hybridization, which in this case, may be indicative of increased abundance of the undesired phases and lack of uniformity thoughout the crystalline structure of the sample. $BiFeO_3$ adopts an octahedral hybridization for the central Fe atom, while $Bi_{25}FeO_{39}$ has a tetragonal arrangement; $Bi_2Fe_4O_9$ adopts both and is considered to be an isostructural compound, where the Fe atoms is central to two different unit cells.[80] In the first cell, Fe_1O_4, Fe is surreounded by four O atoms in a tetrahedral arrangement, while the second cell, Fe_2O_6, is octohedral. The increase in pre-edge peak intensity suggested increased abundance of nonuniform hybridized orbitals. Thus, the XANES results found in this study correlated to intermediate structures as the $BiFeO_3$ phase was converted to $Bi_{25}FeO_{39}$ and $Bi_2Fe_4O_9$.

3.2 Macroscopic analysis of morphological and structural characteristics

The results of N_2 physisorption showed unique trends in surface area for all three catalysts as a result of milling time (Fig. 3A). The surface area of $BaTiO_3$ increased up to 5 h with a maximum surface area of 9.4 $m^2\ g^{-1}$. $BaTiO_3$ had a surface area of 6.8 $m^2\ g^{-1}$ after 1 h and 2 h of milling, while the commercial catalyst had the lowest initial surface area of 3.3 $m^2\ g^{-1}$. The surface area of $NaNbO_3$ showed an increase in the first 1 h of milling (10.4 $m^2\ g^{-1}$), remained stable after 2 h, then significantly fell after 5 h (3.4 $m^2\ g^{-1}$). By contrast, the surface area for the commercial $NaNbO_3$ catalyst was much lower at 0.9 $m^2\ g^{-1}$. The surface area of $BiFeO_3$ remained stable throughout milling at 1 $m^2\ g^{-1}$, which suggested that extended milling did not have a significant impact on the surface area of this catalyst.

The particle sizes of the mechanochemically synthesized catalysts as determined by TEM image analysis averaged 250 nm or smaller in diameter, while that of the commercial catalysts averaged more than 400 nm in diameter (Fig. 3B and Fig. S14–S16). With extended milling, the particle size of $BaTiO_3$ increased from 36 nm after 1 h to 178 nm after 5 h. Commercial $BaTiO_3$ had an average diameter of 482 nm. For $NaNbO_3$ the initial size after 1 h was 54 nm, which increased to 75 nm after 5 h. Commercial $NaNbO_3$ had an average diameter of 426 nm. The average particle size of $BiFeO_3$ remained steady between 220–250 nm from 1 h to 5 h of milling, indicating that extended milling had a minimal impact. Results for pore diameter and pore volume can be found in the SI (Fig. S8) while histograms of all particle sizes can be found in Fig. S14–S16.

The TEM micrographs of mechanochemically synthesized $BaTiO_3$ and $NaNbO_3$ contained areas in which parallel lattice plains were clearly visible, whereas commercial $BaTiO_3$ and $NaNbO_3$ contained less defined features (Fig. 4). The observable crystalline domains for the milled $BaTiO_3$ and $NaNbO_3$ imply strong crystallinity, which is expected to correlate to greater conductivity. This conductivity allowed for a more efficient transfer of electricity throughout the catalyst structure, due to greater ordering, resulting in enhanced electron movement. Additionally, there were distinct difference in particle size between the commercial and milled $BaTiO_3$ and $NaNbO_3$ (Fig. S14 and S15). Commercial $NaNbO_3$ had large particles spanning from 100 nm up to 1600 nm in diameter, while the milled $NaNbO_3$ showed a greater consistency of square-like particles ranging from roughly 25–150 nm in diameter. Similarly, commercial $BaTiO_3$ consisted of particles ranging from 100 nm to 1100 nm, while the mechanochemically synthesized particles did not exceed 200 nm until after 2 h of milling. These histograms (Fig. S14–S16) demonstrate that mechanochemical synthesis of the piezoelectric catalysts results in more uniform particle sizes and overall higher surface area, leading to a greater number of exposed active sites.

TEM images of all mechanochemically synthesized samples of $BaTiO_3$, $NaNbO_3$ and $BiFeO_3$ can be found in Fig. S11–S13. For $BiFeO_3$ HM1C parallel lattice plains were clearly visible throughout the particle structure (Fig. S13B), congruent with observations made for $BaTiO_3$ and $NaNbO_3$ in Fig. 4. Additionally, SEM images depicting the morphological differences and comparative surface roughness between the commercial and mechanochemically synthesized $BaTiO_3$ and $NaNbO_3$ catalysts are shown in Fig. S9 and S10.

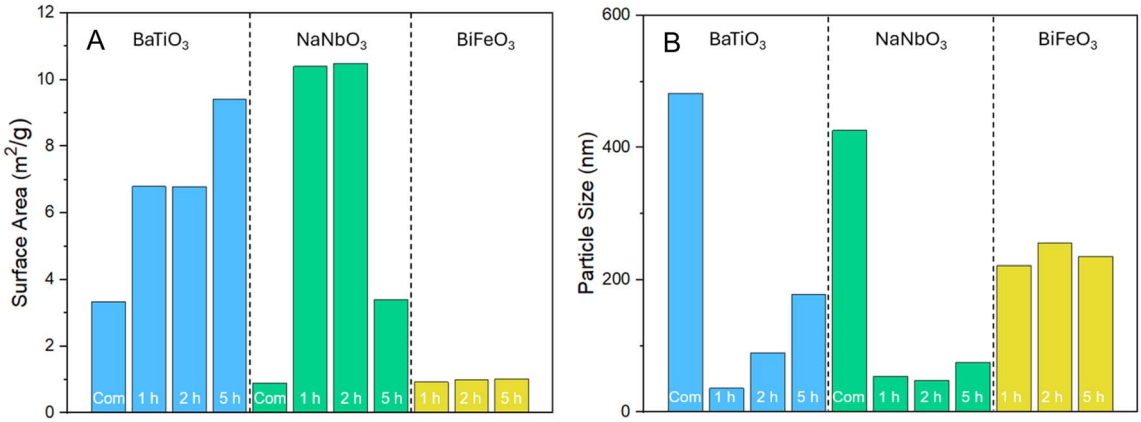

Fig. 3 (A) Surface area based on N_2 physisorption results for the three catalysts. (B) Average particle size for $BaTiO_3$, $NaNbO_3$ and $BiFeO_3$ based on TEM images.

Open Access Article. Published on 28 August 2025. Downloaded on 10/9/2025 2:34:38 PM.
This article is licensed under a Creative Commons Attribution-NonCommercial 3.0 Unported Licence.

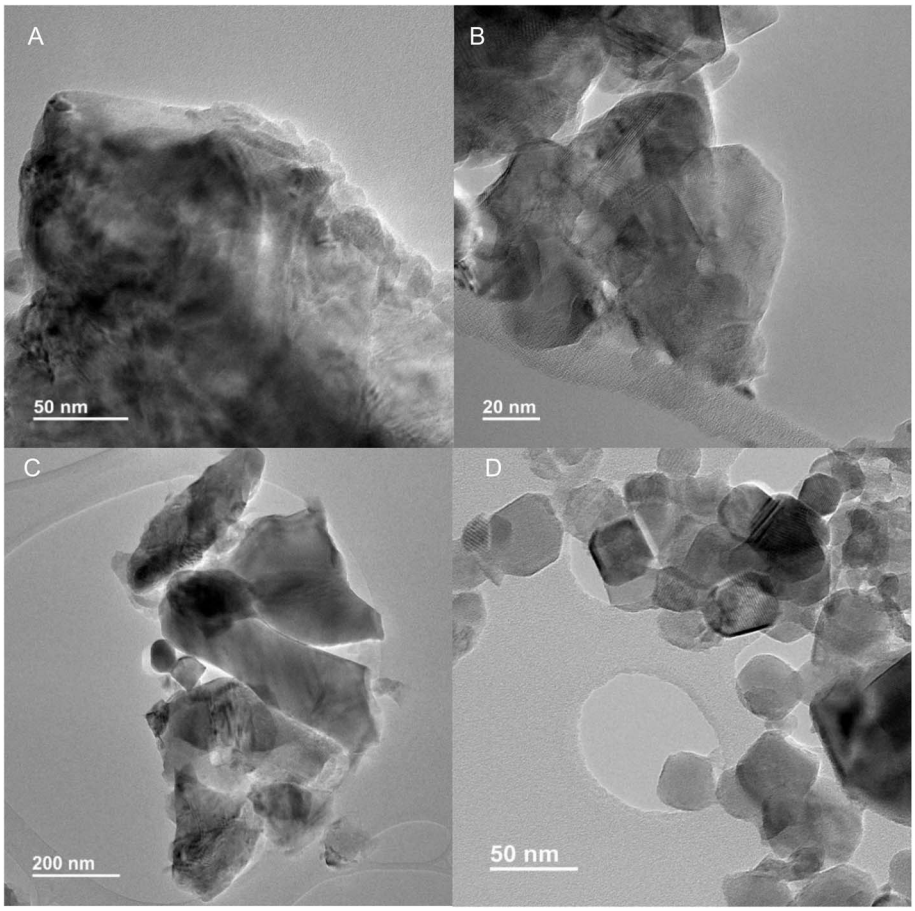

Fig. 4 TEM images for commercial $BaTiO_3$ (A) at a 50 nm scale and HM1C $BaTiO_3$ (B) at a 20 nm scale. TEM images for commercial $NaNbO_3$ (C) at a 200 nm scale and HM2C $NaNbO_3$ (D) at a 50 nm scale.

3.3 Reactivity and performance of an arylation reaction

The arylation reaction of 4-nitrobenzenediazonium tetrafluoroborate and furan to produce 2-(4-nitrophenyl) furan is depicted in Scheme 1. The diazonium salt, 4-nitrobenzenediazonium tetrafluoroborate, was the limiting reactant, whereas furan was used in 15-fold excess due to its high volatility (boiling point: 31 °C). The arylation involved the elimination of N_2 from the diazonium salt. The pathway for side product formation is also shown in Scheme 1, where the main side product was 4,4′-dinitrobiphenyl. Kubota *et al.*[12] used TEMPO as a well-established radical trap[82] to establish that the aryl coupling follows a radical-mediated arylation mechanism.

Control experiments included milling 4-nitrobenzenediazonium tetrafluoroborate alone (Fig. S23) and milling the salt with furan (Fig. 5). The first experiment showed that when the salt was milled alone, only 70% was recollected after milling. This was due to salt decomposition during milling, which was visible upon opening the vessel after the reaction completed. When the salt was milled with furan only, roughly 50% of the salt remained and 12% of 2-(4-nitrophenyl) furan was produced. Once the seal of the vessel was broken, a pressure release ensued as particle matter escaped the vessel and dissipated. The pressure release indicated that the salt partially decomposed to gaseous components, but because this reaction was conducted in a closed milling vessel, the gaseous products could not be collected for quantitative analysis.

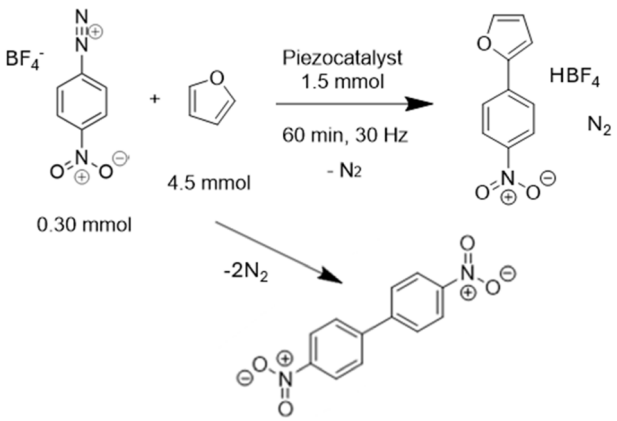

Scheme 1 Arylation of 4-nitrobenzenediazonium tetrafluoroborate and furan, resulting in 2-(4-nitrophenyl) furan as the main product.

The low conversion of the diazonium salt and 12% yield of 2-(4-nitrophenyl) furan demonstrated that a catalyst was necessary to facilitate the radical mediated arylation reaction. The

 © 2025 The Author(s). Published by the Royal Society of Chemistry

Open Access Article. Published on 28 August 2025. Downloaded on 10/9/2025 2:34:38 PM.
This article is licensed under a Creative Commons Attribution-NonCommercial 3.0 Unported Licence.

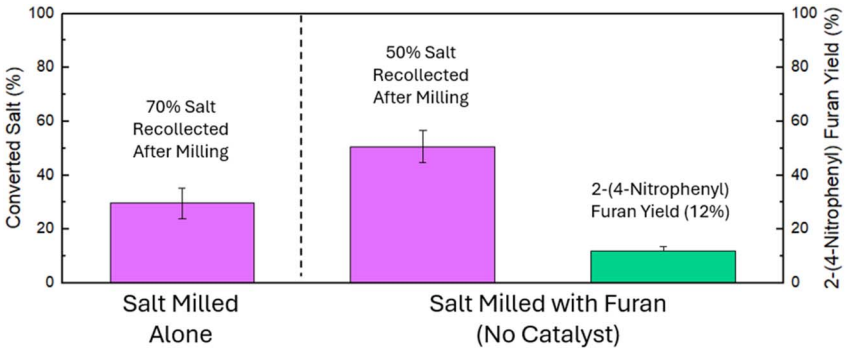

Fig. 5 HPLC for control experiments without a catalyst present.

$BaTiO_3$ samples that were milled for 1 h during synthesis produced the highest yield of 2-(4-nitrophenyl) furan at 40% (Fig. 6). Lower yields of 33% and 31% were observed for the catalysts milled for 2 and 5 h during their synthesis, respectively. The commercial catalyst produced 2-(4-nitrophenyl) furan with a yield of 25%, which was lower than all mechanochemically synthesized samples of $BaTiO_3$. This activity correlated to XAS findings specifically, where $BaTiO_3$ prepared *via* 1 h of synthesis milling had the strongest pre-edge feature, and therefore the highest relative abundance of the P_{4mm} anisotropic phase.

Using $NaNbO_3$, the conversion of 4-nitrobenzenediazonium tetrafluoroborate increased steadily with increased synthesis milling time from 0.5 h (38% yield 2-(4-nitrophenyl) furan) to 2 h (44% yield) followed by a decrease in activity for the sample milled for 5 h (37% yield) (Fig. 6). The low variation in yields (only 7%) are in line with the XRD analysis that showed that $NaNbO_3$ maintained a relatively stable structure and piezoelectric potential with extended synthesis milling. The fresh commercial catalyst gave a 19% yield, while the calcined commercial catalyst yielded 31%. As shown by XRD (Fig. S4), the commercial $NaNbO_3$ was not yet fully formed and required additional heating and milling to reach a pure $NaNbO_3$ phase with no Nb_2O_5 present.

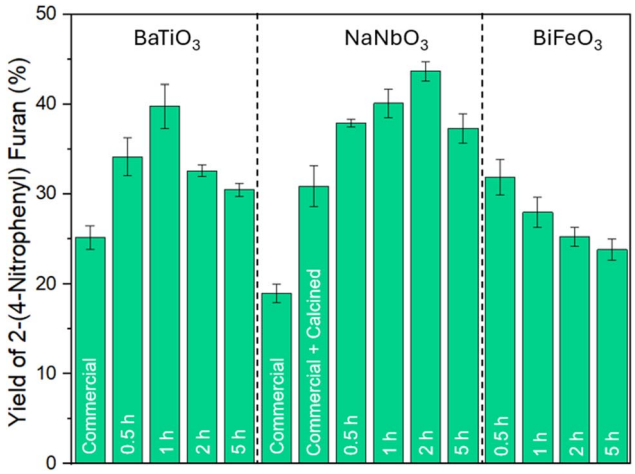

Fig. 6 2-(4-Nitrophenyl) furan yields from the arylation of 4-nitrobenzenediazonium tetrafluoroborate with furan to over $BaTiO_3$, $NaNbO_3$ and $BiFeO_3$ (C).

The HM0.5C catalyst was most productive for $BiFeO_3$, which produced a 32% yield, followed by a decrease for the samples with synthesis milling times of 1 h (28%), 2 h (25%), and 5 h (24%), respectively (Fig. 6). This trend is in agreement with the observation of increasing amounts of $Bi_{25}FeO_{40}$ and $Bi_2Fe_4O_9$ by XRD, indicating that 0.5 h of synthesis milling produced the purest and therefore most active catalyst. Conversion over all catalysts can be found in Section S2.3 (Fig. S22), while ^{1}H NMR spectra and product analysis can be found in Section S2.2 (Fig. S17–S21).

4. Discussion

4.1 Descriptors for catalyst performance

The activity of the piezoelectric catalysts was determined by a combination of factors including the abundance and specific activity of piezoelectric phases, which can be tracked by their shifting crystallinity and morphology throughout the synthesis milling process. For $BaTiO_3$, XRD and XAS provided the most insightful findings. The shift from the anisotropic P_{4mm} structure to a centrosymmetrical P_{m3m} lattice was identifiable through the increased peak intensity at 45° *via* XRD. XAS strongly correlated to these findings (Fig. 2A and B) and demonstrated the highest pre-edge peak intensity, congruent with the highest abundance of the anisotropic P_{4mm} phase, after 1 h of synthesis milling; these results aligned with the arylation reactivity of $BaTiO_3$ in Fig. 6, and the correlation is plotted in Fig. 7. This indicated that $BaTiO_3$ exhibited efficient charge separation.

By comparison, the surface area increased throughout 5 h of milling, which indicated that size reduction of particles occurred, but this was coupled with the formation of centrosymmetric cubic unit cells and, thus, catalyst deactivation. The mechanochemically synthesized $BaTiO_3$ surpassed the yield of the arylation product over the commercial sample by 20%, likely because the synthesized $BaTiO_3$ had well defined lattice plains, as observed by TEM in Fig. 4. The commercial sample lacked observable crystalline domains and was therefore less conductive and crystalline when compared to the mechanochemically synthesized sample. The commercial sample also had half the

Open Access Article. Published on 28 August 2025. Downloaded on 10/9/2025 2:34:38 PM.
This article is licensed under a Creative Commons Attribution-NonCommercial 3.0 Unported Licence.

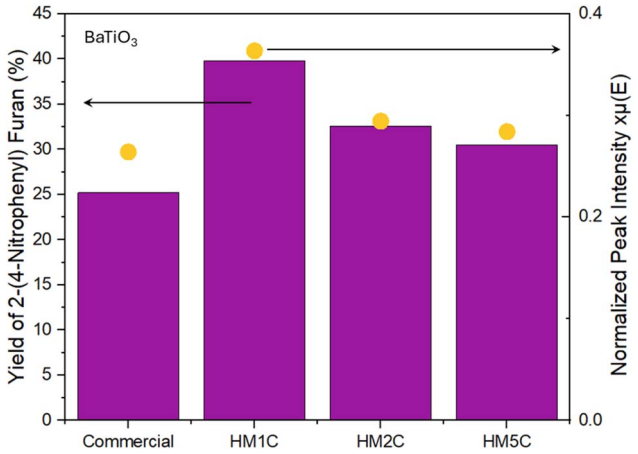

Fig. 7 Changes in 2-(4-nitrophenyl) furan yield for $BaTiO_3$ catalysts compared to changes in normalized XAS pre-edge peak intensity.

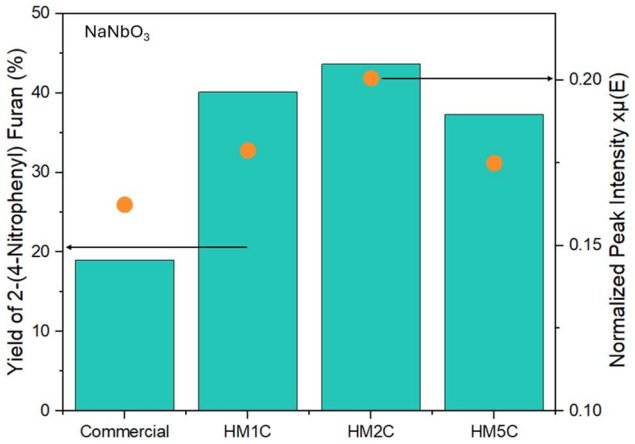

Fig. 8 Changes in 2-(4-nitrophenyl) furan yield for $NaNbO_3$ catalysts compared to changes in normalized XAS pre-edge peak intensity.

surface area as the mechanochemically milled particles, suggesting fewer active sites were initially accessible on the larger particles. Overall, the characterization and test reaction confirm that the $BaTiO_3$ sample that was mechanochemically synthesized for 1 h was the most effective out of all $BaTiO_3$ samples because it had the greatest abundance of the desired P_{4mm} anisotropic phase.

$NaNbO_3$ demonstrated very similar behavior to $BaTiO_3$, and reactivity for this piezoelectric material also scaled with the pre-edge peak intensity of the sample, correlating to greater hybridization of the $Nb_{(4d)}$ and $O_{(2p)}$ orbitals and a greater abundance of the orthorhombic C_{cmm} phase (Fig. 8). Because XRD confirmed that both C_{cmm} and $P_{12/m1}$ phases were present and anisotropic, decreases in the catalytic activity of this catalyst could not primarily be attributed to changes in crystallinity. The shift from C_{cmm} to $P_{12/m1}$ coupled with a reduction in surface area, presumably by sintering, resulted in less active catalysts with excessive milling time during synthesis. This shift in crystal phase was also identified by XAS (Fig. 2C and D), and a significant decrease in peak intensity was observed from 2 h of synthesis milling to 5 h. The HM2C sample had an intensity of 0.201, which fell to 0.175 for HM5C; the intensity for HM1C fell in between these two values at 0.179. As shown by Fig. 8, these values strongly correlated to the yields obtained for 2-(4-nitrophenyl) furan. The analysis of surface area gave greater insight into the reactivity observed for the arylation reaction, where $NaNbO_3$ synthesized for 1 h and 2 h were the most highly reactive catalysts and had surface areas of 10.4 and 10.5 $m^2\ g^{-1}$ respectively. This resulted in yields of 41% and 44% 2-(4-nitrophenyl) furan. After 5 h, particle sintering began to occur, and the surface area fell to 3.4 $m^2\ g^{-1}$, followed by a decrease in yield to 37%. By contrast, the commercial $NaNbO_3$ had the lowest initial surface area and pre-edge peak intensity at 0.9 $m^2\ g^{-1}$ and 0.162 respectively and achieved a 19% yield of 2-(4-nitrophenyl) furan.

Like $BaTiO_3$, $NaNbO_3$ outperformed its commercial counterpart, doubling the yield. As shown in Fig. S4, the untreated catalyst did not have a fully formed crystal structure, so calcination was performed in an attempt to remedy this issue. After heating, characteristic peaks for $NaNbO_3$ became more prominent, but it was not until the catalyst was milled that the $P_{mmn:2}$ crystal structure was identifiable. The larger particle size of the commercial $NaNbO_3$ catalyst was also confirmed through TEM imaging (Fig. 3 and 4). Physisorption showed that the surface area of the commercial catalyst was one tenth that of the mechanochemically synthesized catalyst, and TEM images demonstrated that the particle size (up to 1600 nm diameter) was the largest of all the analyzed piezoelectric catalysts. Fig. 4 also depicts the uniform rounded cubic structure of the mechanochemically synthesized particles, whereas the commercial $NaNbO_3$ sample had much larger particles that lacked observable lattice plains, similar to $BaTiO_3$. Calcination improved the yield of 2-(4-nitrophenyl) furan over commercial $NaNbO_3$ by roughly 12%, but it still underperformed when compared to the worst performing mechanochemically synthesized $NaNbO_3$ catalyst.

For $BiFeO_3$, the reactivity of the catalyst directly correlated to the increase in the abundance of inactive phases as observed by the XRD results (Fig. 9). The undesired $Bi_{25}FeO_{40}$ and $Bi_2Fe_4O_9$ phases were already apparent after the first 30 min of synthesis milling. As the abundance of these phases increased, conversion fell, and yields decreased for the arylation reaction from 32% to 24%. While extended milling had a significant impact on the crystallinity of $BiFeO_3$, changes in the surface area and particle size were negligible.

4.2 Kinetics and reaction mechanisms

To compare the kinetic behaviors and reaction mechanistics between the catalyst, the synthesis of 2-(4-nitrophenyl) furan ($O_2NPhC_4H_4O$) and 4,4′-dinitrobiphenyl ($(O_2NPh)_2$) from 4-nitrobenzenediazonium tetrafluoroborate ($(O_2NPhN_2)^+BF_4^-$) and furan (C_4H_4O) was performed over the same loading of HM1C catalyst for $BaTiO_3$ and $BiFeO_3$ and HM2C for $NaNbO_3$. The desired reaction pathway is described by the following reaction sequence according to Kubota *et al.*:[12]

$$\text{ehp} \rightarrow e^- + h^+ \quad \text{(R1)}$$

 © 2025 The Author(s). Published by the Royal Society of Chemistry

Open Access Article. Published on 28 August 2025. Downloaded on 10/9/2025 2:34:38 PM.
This article is licensed under a Creative Commons Attribution-NonCommercial 3.0 Unported Licence.

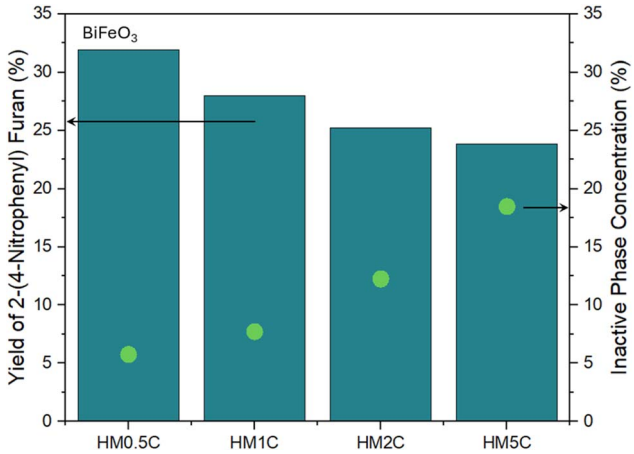

Fig. 9 Changes in 2-(4-nitrophenyl) furan yield for $BiFeO_3$ catalysts compared to increasing composition of the $Bi_4Fe_2O_9$ and $Bi_{25}FeO_{39}$ phases as determined by XRD.

$$(O_2NPhN_2)^+BF_4^- + e^- \xrightarrow{k_2} (O_2NPh)^\bullet + BF_4^- + N_2\uparrow \quad (R2)$$

$$(O_2NPh)^\bullet + C_4H_4O \xrightarrow{k_3} O_2NPhC_4H_4O^\bullet \quad (R3)$$

$$O_2NPhC_4H_4O^\bullet + h^+ \xrightarrow{k_4} O_2NPhC_4H_4O^+ \quad (R4)$$

$$O_2NPhC_4H_4O^+ + BF_4^- \underset{k_{-5}}{\overset{k_5}{\rightleftarrows}} O_2NPhC_4H_4O + HBF_4 \quad (R5)$$

$$2(O_2NPh)^\bullet \xrightarrow{k_6} (O_2NPh)_2 \quad (R6)$$

The conversion of 4-nitrobenzenediazonium tetrafluoroborate as well as the rate of formation and the yield of 2-(4-nitrophenyl) furan and 4,4′-dinitrobiphenyl observed for each catalyst are plotted against time in Fig. 10.

The conversion of 4-nitrobenzenediazonium tetrafluoroborate reached approximately 90% over all three catalysts after 60 minutes of milling (Fig. 10A). The measured rate of formation for 2-(4-nitrophenyl) furan for all catalysts are represented in Fig. 10C. Specifically, the formation of 2-(4-nitrophenyl) furan was shown to follow a first order in 4-nitrobenzenediazonium tetrafluoroborate when applied to $BaTiO_3$, whereas $NaNbO_3$ and $BiFeO_3$ followed zero-order and $\frac{1}{2}$-order in 4-nitrobenzenediazonium tetrafluoroborate, respectively. Similarly, the measured rate of formation of 4,4′-dinitrobiphenyl in Fig. 10E followed first-order kinetics observed for $BaTiO_3$ and $BiFeO_3$, whereas $NaNbO_3$ exhibited a zero-order in 4-nitrobenzenediazonium tetrafluoroborate for this reaction. In addition, the kinetics provided insight into the limiting factors of the arylation reaction of 2-(4-nitrophenyl) furan with 4-nitrobenzenediazonium tetrafluoroborate. To test potential mechanisms, rate equations were derived based on various assumptions. The protonation step (eqn (R5)) was assumed to be in quasi-equilibrium, with equilibrium K_5 (see eqn (SEQ1)). Due to the high reactivity of radicals, the pseudo-steady-state hypothesis (PSSH) was applied to assume that the concentration of the nitrophenyl ($(O_2NPh)^\bullet$) and the 2-(4-nitrophenyl) furan radicals ($O_2NPhC_4H_4O^\bullet$) remained constant (see eqn (SEQ2)). With furan in large excess, the overall rate expression was assumed to be independent of the furan concentration, *i.e.*, quasi zero-order (see eqn (SEQ3)).

For the formation of 2-(4-nitrophenyl) furan, the reaction rate ($r_{O_2NPhC_4H_4O}$) and reaction order differed among catalysts due to variations in piezoelectric properties and the availability of charge carriers. $BaTiO_3$ exhibited a first-order dependence on the diazonium salt. Under the pseudo-steady-state hypothesis (PSSH), the concentration of the nitrophenyl radical intermediate was shown to be approximated as a function of the diazonium salt and electron concentration (see eqn (SEQ6)). The latter was found to be governed by the strength of the piezoelectric field E, which is determined by intrinsic material properties specifically, the piezoelectric charge coefficient d, the mechanical stress σ, and the dielectric constant (or relative permittivity) ε $\left(E = \frac{d\sigma}{\varepsilon}\right)$.[21,22] The resulting electron–hole pair concentration ($[e^-]/[h^+]$) was treated as a material-specific parameter (k^*_{Mat}) ($[e^-] = [h^+] \propto k^*_{Mat}(E)$), which encapsulates the effective concentration of charge carriers generated under a given field strength. Substituting this into the rate law yields a first-order dependence on the diazonium salt ($r_{O_2NPhC_4H_4O,BaTiO3} = k_{C,BaTiO_3,app}[(O_2NPhN_2)^+BF_4^-]$), in which the apparent rate constant can be expressed as $k_{C,BaTiO_3,app} = k_2 {k^*_{BaTiO_3}}^2$ (see eqn (SEQ10)).

The rate of formation of 2-(4-nitrophenyl) furan followed zero-order kinetics for $NaNbO_3$ in 4-nitrobenzenediazonium tetrafluoroborate ($r_{O_2NPhC_4H_4O,NaNbO_3} = k_{C,NaNbO_3,app}$), indicating that the reaction rate was independent of the diazonium salt concentration. This behavior is attributed to a rate-limiting step governed by the generation of electron–hole pairs in the piezocatalyst, which occurs more slowly than subsequent transformation steps (see eqn (SEQ12)). As a result, the apparent rate constant $k_{C,NaNbO_3,app}$ is determined primarily by the intrinsic ability of $NaNbO_3$ to generate charge carriers under mechanical activation ($k_{C,NaNbO_3,app} = k_{C,NaNbO_3} k^*_{NaNbO_3}$).

$BiFeO_3$ demonstrated a half-order in 4-nitrobenzenediazonium tetrafluoroborate ($r_{O_2NPhC_4H_4O,BiFeO_3} = k_{C,BiFeO_3,app}[(O_2NPhN_2)^+BF_4^-]^{1/2}$), (see eqn (SEQ17)). The radical concentration $[(O_2NPh)^\bullet]$ was derived using the pseudo-steady-state hypothesis (PSSH) and shown to be proportional to $[(O_2NPhN_2)^+BF_4^-]^{1/2}$ (see eqn (SEQ15)). Applying PSSH to the concentration of the 2-(4-nitrophenyl) furan radical species $[O_2NPhC_4H_4O^\bullet]$ led to the reaction rate follows a half-order dependence on the diazonium salt concentration (see eqn (SEQ16) and (SEQ17)). This fractional order reflects the enhanced charge carrier availability due to its relatively high charge density. The lower reaction rate over $BiFeO_3$ compared to other materials, suggested that the piezocatalytic activity of $BiFeO_3$ tends to be limited because a significant fraction of it is present in inactive phases such as $Bi_{25}FeO_{40}$ and $Bi_2Fe_4O_9$ (see Section 4.1).

The formation of 4,4′-dinitrobiphenyl over $BaTiO_3$ followed first-order kinetics ($r_{(O_2NPh)_2,BaTiO_3} =$

Open Access Article. Published on 28 August 2025. Downloaded on 10/9/2025 2:34:38 PM.
This article is licensed under a Creative Commons Attribution-NonCommercial 3.0 Unported Licence.

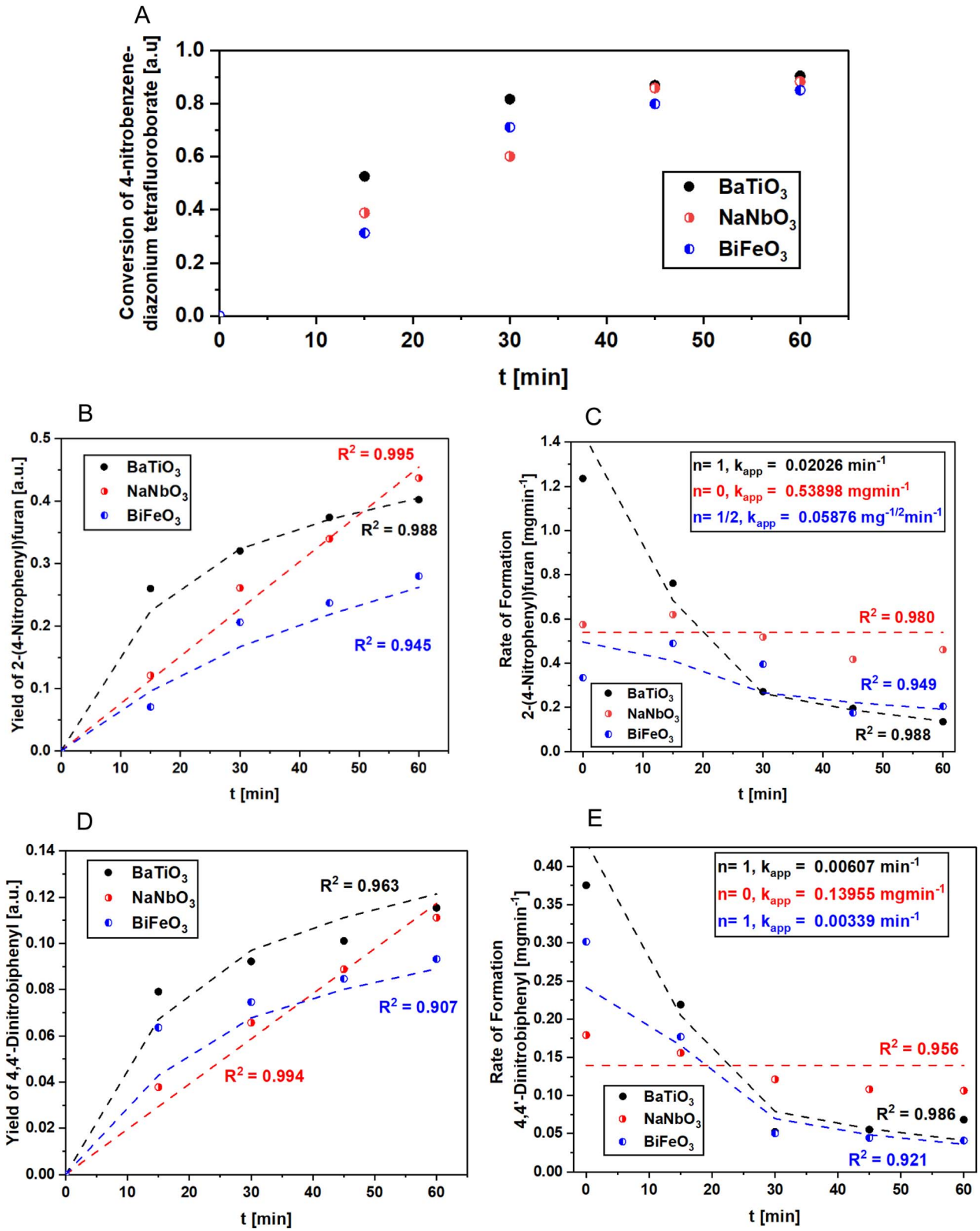

Fig. 10 Temporal change of (A) conversion of 4-nitrobenzenediazonium tetrafluoroborate (B) yield and (C) rate of formation of 2-(4-nitrophenyl)furan (D) yield and (E) rate of formation of 4,4′-dinitrobiphenyl, (the dashed lines in subfigures (b), (c), (d), and (e) represents the kinetic equations that were fitted to the mass of 4-nitrobenzenediazonium tetrafluoroborate).

 © 2025 The Author(s). Published by the Royal Society of Chemistry

Open Access Article. Published on 28 August 2025. Downloaded on 10/9/2025 2:34:38 PM.
This article is licensed under a Creative Commons Attribution-NonCommercial 3.0 Unported Licence.

$k_{E,BaTiO_3,app}[(O_2NPhN_2)^+BF_4^-]$) (see eqn (SEQ11)). This first-order dependence appears as the $[(O_2NPh)^\bullet]$ remains low ($[(O_2NPh)^\bullet] \approx 0$), allowing its quadratic term in the rate expression to be approximately close to the value of the first-order term ($[(O_2NPh)^\bullet] \approx [(O_2NPh)^\bullet]^2$) (see eqn (SEQ11)). Since the rate of formation of 4,4′-dinitrobiphenyl was proportional to $[(O_2NPh)^\bullet]^2$, substituting this expression yields an overall first-order dependence on the diazonium salt (see eqn (SEQ13)). $NaNbO_3$, in contrast, displayed zero-order kinetics ($r_{(O_2NPh)_2,NaNbO3} = k_{E,NaNbO_3,app}$) because the rate was limited by the availability of charge carriers (see eqn (SEQ13)). $BiFeO_3$ exhibited first-order kinetics ($r_{(O_2NPh)_2,BiFeO_3} = k_{E,BiFeO_3,app}[(O_2NPhN_2)^+BF_4^-]$), indicating that the rate of dimer formation scaled with the concentration of the nitrophenyl radicals (see eqn (SEQ18)). The apparent reaction rate constants for the formation of 2-(4-nitrophenyl) furan ($k_{C,app}$) and of 4,4′-dinitrobiphenyl ($k_{E,app}$) for all cases are provided in Fig. 10C and E. The calculated yields of 2-(4-nitrophenyl) furan and 4,4′-dinitrobiphenyl aligned well with measured yields, demonstrating an accurate estimation of the reaction rate across all three catalysts (Fig. 10B and D).

The present results show that several descriptors affect the performance of the piezoelectric catalysts in this study, which plays into the reaction rates by influencing the concentration of electrons available for the piezocatalytic activity. While a sufficient surface area is needed for reactants to interact with the catalyst, the catalyst also needs to be able to separate charges, which depends on the presence of piezoelectric phases and properties of these phases, such as piezoelectric charge coefficient, electromechanical coupling factor, and the dielectric constant.[81] In the present case, the formation of 2-(4-nitrophenyl) furan as well as 4,4′-dinitrobiphenyl was favored over catalysts with high surface area and abundance of piezoelectric phases. $NaNbO_3$ thus had the highest yield for 2-(4-nitrophenyl) production (44%), correlating with its stable structure and high surface area with milling time. Therefore, it is essential to consider both microscopic properties (*e.g.*, coupling factor, crystal structure) and macroscopic characteristics (*e.g.*, surface area) to ensure optimal catalytic performance. The interplay between these factors can significantly influence reaction kinetics, leading to more complex mechanistic behavior. While the radical nature of the aryl coupling mechanism has not been directly demonstrated in this study, our kinetic observations are consistent with the mechanism of radical-mediated arylation involving aryl diazonium salts reported by Kubota *et al.*[12] The use of radical traps such as TEMPO is a well-established approach for probing radical mechanisms,[82] and the results of the Kubota study provide strong support for the intermediacy of aryl radicals under related conditions.[12]

Conclusion

During mechanochemical processes, compression of piezoelectric catalysts like $BaTiO_3$, $NaNbO_3$, and $BiFeO_3$ creates ensembles of electrons and holes that can be leveraged to drive organic reactions, such as the arylation of furan with 4-nitrobenzenediazonium tetrafluoroborate. Active structures are meta-stable and are subject to shifts in phase composition with extended milling times. Piezoelectric catalysts with high activity and high levels of crystallinity can be obtained with mechanochemical synthesis within 2 h. Kinetic measurements revealed that the synthesis of 2-(4-nitrophenyl) furan and 4,4′-dinitrobiphenyl from 4-nitrobenzenediazonium tetrafluoroborate and furan over $BaTiO_3$ exhibited first-order kinetics in 4-nitrobenzenediazonium tetrafluoroborate for both processes due to efficient electron–hole separation, while $NaNbO_3$ followed zero-order kinetics due to the limited availability of electrons and holes that are required to drive the reaction. Despite its limited charge separation, $NaNbO_3$ achieved the highest yield (44%) of 2-(4-nitrophenyl) furan. $BiFeO_3$ showed a half-order in 4-nitrobenzenediazonium tetrafluoroborate for 2-(4-nitrophenyl) furan formation, and first-order kinetics for 4,4′-dinitrobiphenyl formation as a result of the high charge carrier density that enhanced electron transfer.

Overall, piezocatalytic activity appears to be governed by the surface area of anisotropic phases and their specific activity. The latter can be expressed as the overall piezoelectric field strength of each catalyst. However, field strength cannot be directly measured during the mechanochemical process in this work. The abundance of these phases was observed in a different way for each catalyst. The activity of $BaTiO_3$ was directly proportional to XANES pre-edge intensity, which was indicative of the abundance of the anisotropic P_{4mm} tetragonal phase. The activity of $NaNbO_3$ also scaled with the abundance of anisotropic phases, but it also increased with increasing surface area, demonstrating the need for small piezoelectric particles. By contrast, the activity of $BiFeO_3$ decreased as the abundance of non-piezoelectric $Bi_4Fe_2O_9$ and $Bi_{25}FeO_{39}$ phases increased. These findings underscore the necessity of considering multiple material properties in catalyst design to optimize reaction kinetics and product selectivity. This work provides guidance for designing mechanocatalytic processes, wherein the piezoelectric catalyst can be efficiently activated *via* mechanical impacts. The energy provided by milling coupled with optimal crystallographic features for these materials created active species for radical reactions.

Conflicts of interest

The authors declare no competing financial interest.

Data availability

Raw data and original files from instrument software can be obtained from the authors upon request.

Additional data supporting this article have been included as part of the SI. Supplementary information: Analytical data including XRD, N_2 physisorption analysis of pore size and volume, SEM and TEM images with histograms, a schematic for side product formation of the arylation reaction, derivation of kinetic rate equations, proton ^{1}H NMR spectra, conversion data and FTIR spectra. See DOI: **https://doi.org/10.1039/d5mr00062a**.

Open Access Article. Published on 28 August 2025. Downloaded on 10/9/2025 2:34:38 PM.
This article is licensed under a Creative Commons Attribution-NonCommercial 3.0 Unported Licence.

Acknowledgements

This research was supported by BASF. This research used Inner Shell Spectroscopy beamline (ISS, 8-ID) of the National Synchrotron Light Source II, a U.S. Department of Energy (DOE) Office of Science User Facility operated for the DOE Office of Science by Brookhaven National Laboratory under Contract No. DE-SC0012704.

References

1 A. W. Tricker, G. Samaras, K. L. Hebisch, M. J. Realff and C. Sievers, *Chem. Eng. J.*, 2020, **382**, 122954.
2 J. L. Howard, Q. Cao and D. L. Browne, *Chem. Sci.*, 2018, **9**, 3080–3094.
3 L. Takacs, *Chem. Soc. Rev.*, 2013, **42**, 7649–7659.
4 P. F. M. de Oliveira, R. M. Torresi, F. Emmerling and P. H. C. Camargo, *J. Mater. Chem. A*, 2020, **8**, 16114–16141.
5 A. P. Amrute, J. De Bellis, M. Felderhoff and F. Schuth, *Chemistry*, 2021, **27**, 6819–6847.
6 C. Xu, S. De, A. M. Balu, M. Ojeda and R. Luque, *Chem. Commun.*, 2015, **51**, 6698–6713.
7 A. W. Tricker, M. J. Stellato, T. T. Kwok, N. S. Kruyer, Z. Wang, S. Nair, V. M. Thomas, M. J. Realff, A. S. Bommarius and C. Sievers, *ChemSusChem*, 2020, **13**, 4624–4632.
8 F. Schüth, R. Rinaldi, N. Meine, M. Käldström, J. Hilgert and M. D. K. Rechulski, *Catal. Today*, 2014, **234**, 24–30.
9 M. D. Kaufman Rechulski, M. Käldström, U. Richter, F. Schüth and R. Rinaldi, *Ind. Eng. Chem. Res.*, 2015, **54**, 4581–4592.
10 M. Kessler and R. Rinaldi, *Front. Chem.*, 2021, **9**, 816553.
11 V. S. Nguyen, Y. Chang, E. V. Phillips, J. A. DeWitt and C. Sievers, *ACS Sustainable Chem. Eng.*, 2023, **11**, 7617–7623.
12 K. Kubota, Y. Pang, A. Miura and H. Ito, *Science*, 2019, **366**, 1500–1504.
13 F. Fischer, K. J. Wenzel, K. Rademann and F. Emmerling, *Phys. Chem. Chem. Phys.*, 2016, **18**, 23320–23325.
14 X. Liu, Y. Li, L. Zeng, X. Li, N. Chen, S. Bai, H. He, Q. Wang and C. Zhang, *Adv. Mater.*, 2022, **34**, e2108327.
15 S. Amirjalayer, H. Fuchs and D. Marx, *Angew Chem. Int. Ed. Engl.*, 2019, **58**, 5232–5235.
16 F. R. Fan, S. Xie, G. W. Wang and Z. Q. Tian, *Sci. China: Chem.*, 2021, **64**, 1609–1613.
17 S. Tu, Y. Guo, Y. Zhang, C. Hu, T. Zhang, T. Ma and H. Huang, *Adv. Funct. Mater.*, 2020, **30**, 2005158.
18 Y. Feng, L. Ling, Y. Wang, Z. Xu, F. Cao, H. Li and Z. Bian, *Nano Energy*, 2017, **40**, 481–486.
19 X. Wang, Y. Jia, Y. Wang, X. Xu, L. Qin and Z. Wu, *J. Am. Ceram. Soc.*, 2023, **107**, 1682–1690.
20 Y. Liu, H. Y. Xu and S. Komarneni, *Appl. Catal., A*, 2024, **670**, 119550.
21 T. Ikeda, *Fundamentals of Piezoelectricity*, Oxford University Press, 1996.
22 O. M. M. Manfra, *J. Appl. Phys.*, 2004, **95**, 6414–6419.
23 K. Yoshii, Y. Yoneda, I. Jarrige, T. Fukuda, Y. Nishihata, C. Suzuki, Y. Ito, T. Terashima, S. Yoshikado and S. Fukushima, *J. Phys. Chem. Solids*, 2014, **75**, 339–343.
24 Z. Lazarevi, N. Romcevi, M. Vijatovi, N. Paunovi, M. Romcevi, B. Stojanovi and Z. Dohcevi Mitrovi, *Acta Phys. Pol. A*, 2009, **115**, 808–810.
25 W. Somphon and S. Srilomsak, *Adv. Mater. Res.*, 2008, **55–57**, 157–160.
26 P. Phaktapha, J. Jutimoosik, A. Bootchanont, P. Kidkhunthod, S. Rujirawat and R. Yimnirun, *Integr. Ferroelectr.*, 2017, **177**, 74–78.
27 C. Correas, T. Hungría and A. Castro, *J. Mater. Chem.*, 2011, **21**, 3125–3132.
28 T. Higuchi, Y. S. Liu, P. Yao, P. A. Glans, J. Guo, C. Chang, Z. Wu, W. Sakamoto, N. Itoh, T. Shimura, T. Yogo and T. Hattori, *Phys. Rev. B: Condens. Matter Mater. Phys.*, 2008, **78**, 085106.
29 T. Gholam, L. R. Zheng, J. O. Wang, H. J. Qian, R. Wu and H. Wang, *Nanoscale Res. Lett.*, 2019, **14**, 137.
30 T. Higuchi, W. Sakamoto, N. Itoh, T. Shimura, T. Hattori and T. Yogo, *Appl. Phys. Express*, 2008, **1**, 011502.
31 T. Rojac, M. Kosec, B. Malič and J. Holc, *Mater. Res. Bull.*, 2005, **40**, 341–345.
32 J. Koruza, J. Tellier, B. Malič, V. Bobnar and M. Kosec, *J. Appl. Phys.*, 2010, **108**, 113509.
33 B. D. Stojanovic, C. Jovalekic, V. Vukotic, A. Z. Simoes and J. A. Varela, *Ferroelectrics*, 2005, **319**, 65–73.
34 B. D. Stojanovic, A. Z. Simoes, C. O. Paiva-Santos, C. Jovalekic, V. V. Mitic and J. A. Varela, *J. Eur. Ceram. Soc.*, 2005, **25**, 1985–1989.
35 C. Miclea, C. Tanasoiu, I. Spanulescu, C. F. Miclea, A. Gheorghiu, L. Amarande, M. Cioangher, C. T. Miclea and J. Romanian, *Inf. Sci. Technol.*, 2007, **10**, 335–345.
36 M. M. Vijatović, M. R. Vasic, J. D. Bobić, L. M. Živković and B. D. Stojanović, *Process. Appl. Ceram.*, 2008, **2**, 27–31.
37 V. A. Zazhigalov, V. V. Sidorchuk, S. V. Khalameida and L. S. Kuznetsova, *Inorg. Mater.*, 2008, **44**, 641–645.
38 R. Ashiri, *RSC Adv.*, 2016, **6**, 17138–17150.
39 E. Markiewicz, B. Hilczer, M. Błaszyk, A. Pietraszko and E. Talik, *J. Electroceram.*, 2011, **27**, 154–161.
40 A. A. Cristóbal and P. M. Botta, *Mater. Chem. Phys.*, 2013, **139**, 931–935.
41 A. V. Egorysheva, V. D. Volodin, O. G. Ellert, N. N. Efimov, V. M. Skorikov, A. E. Baranchikov and V. M. Novotortsev, *Inorg. Mater.*, 2013, **49**, 303–309.
42 M. Ahmadzadeh, A. Ataie and E. Mostafavi, *J. Alloys Compd.*, 2015, **622**, 548–556.
43 F. Pedro-García, F. Sánchez-De Jesús, C. A. Cortés-Escobedo, A. Barba-Pingarrón and A. M. Bolarín-Miró, *J. Alloys Compd.*, 2017, **711**, 77–84.
44 T. Rojac, O. Masson, R. Guinebretière, M. Kosec, B. Malič and J. Holc, *J. Eur. Ceram. Soc.*, 2007, **27**, 2265–2271.
45 T. Rojac, B. Malič, M. Kosec, M. Połomska, B. Hilczer, B. Zupančič and B. Zalar, *Solid State Ionics*, 2012, **215**, 1–6.
46 H. Z. Akbas, Z. Aydin, F. Guder and S. Turgut, *J. Alloys Compd.*, 2017, **699**, 87–91.

 © 2025 The Author(s). Published by the Royal Society of Chemistry

Open Access Article. Published on 28 August 2025. Downloaded on 10/9/2025 2:34:38 PM.
This article is licensed under a Creative Commons Attribution-NonCommercial 3.0 Unported Licence.

47 Z. Aydin, S. Turgut and H. Z. Akbas, *Powder Metall. Met. Ceram.*, 2018, **57**, 490–497.
48 T. Rojac, M. Kosec, B. Malič and J. Holc, *Sci. Sintering*, 2005, **37**, 61–67.
49 J. Y. Yun, J. H. Jeon and S. J. L. Kang, *Mater. Trans.*, 2008, **49**, 2166–2168.
50 J. H. Jeon, *Curr. Opin. Chem. Eng.*, 2014, **3**, 30–35.
51 T. Hungría, L. Pardo, A. Moure and A. Castro, *J. Alloys Compd.*, 2005, **395**, 166–173.
52 H. A. M. van Hal, W. A. Groen, S. Maassen and W. C. Keur, *J. Eur. Ceram. Soc.*, 2001, **21**, 1689–1692.
53 A. Kondo, S. Hirofumi and K. Sato, *Trans. JWRI*, 2006, **35**, 63–65.
54 S. Ohara, A. Kondo, H. Shimoda, K. Sato, H. Abe and M. Naito, *Mater. Lett.*, 2008, **62**, 2957–2959.
55 I. U. Idehenre, Y. A. Barnakov, S. A. Basun and D. R. Evans, *J. Appl. Phys.*, 2018, **124**, 165501.
56 Z. Dai and Y. Akishige, *Mater. Lett.*, 2012, **88**, 36–39.
57 I. Szafraniak, M. Połomska, B. Hilczer, A. Pietraszko and L. Kępiński, *J. Eur. Ceram. Soc.*, 2007, **27**, 4399–4402.
58 C. Schumacher, J. G. Hernandez and C. Bolm, *Angew. Chem., Int. Ed. Engl.*, 2020, **59**, 16357–16360.
59 F. Effaty, X. Ottenwaelder and T. Friščić, *Curr. Opin. Green Sustainable Chem.*, 2021, **32**, 100524.
60 Y. Wang, Z. Zhang, L. Deng, T. Lao, Z. Su, Y. Yu and H. Cao, *Org. Lett.*, 2021, **23**, 7171–7176.
61 G. Wang, J. Jia, Y. He, D. Wei, M. Song, L. Zhang, G. Li, H. Li and B. Yuan, *RSC Adv.*, 2022, **12**, 18407–18411.
62 K. L. Da Silva, D. Menzel, A. Feldhoff, C. Kübel, M. Bruns, A. Paesano, A. Düvel, M. Wilkening, M. Ghafari and H. Hahn, *J. Phys. Chem. C*, 2011, **115**, 7209–7217.
63 B. Ravel and M. Newville, *J. Synchrotron Radiat.*, 2005, **12**, 537–541.
64 S. Brunauer, P. H. Emmett and E. Teller, *J. Am. Chem. Soc.*, 1938, **60**, 309–319.
65 S. Kudlacik-Kramarczyk, A. Drabczyk, M. Glab, P. Dulian, R. Bogucki, K. Miernik, A. Sobczak-Kupiec and B. Tyliszczak, *Materials*, 2020, **13**, 3275.
66 G. Kozma, K. Lipták, C. Deák, A. Rónavári, A. Kukovecz and Z. Kónya, *Chemistry*, 2022, **4**, 592–602.
67 S. Unruan, M. Unruan, T. Monnor, S. Priya, R. Yimnirun and X. Tan, *J. Am. Ceram. Soc.*, 2015, **98**, 3291–3298.
68 G. Wang, D. Cheng, T. He, Y. Hu, Q. Deng, Y. Mao and S. Wang, *J. Mater. Sci.:Mater. Electron.*, 2019, **30**, 10923–10933.
69 J. Jutimoosik, S. Hunpratub, S. Maensiri, S. Rujirawat and R. Yimnirun, *J. Appl. Phys.*, 2014, **116**, 104105.
70 O. Kamon-in, W. Pattanasiriwisawa, A. Yangthaisong and S. Srilomsak, *J. Phys.: Conf. Ser.*, 2009, **190**, 012082.
71 D. Phuyal, S. Mukherjee, S. Das, S. Jana, K. O. Kvashnina, D. D. Sarma, H. Rensmo, S. M. Buortin and O. Karis, *Europhys. Lett.*, 2018, **124**, 27005.
72 S. Kato, N. Nakajima, S. Yasui, S. Yasuhara, D. Fu, J. Adachi, H. Nitani, Y. Takeichi and A. Anspoks, *Acta Mater.*, 2021, **207**, 116681.
73 G. Panchal, D. K. Shukla, R. J. Choudhary, V. R. Reddy and D. M. Phase, *AIP Conf. Proc.*, 2017, **1832**, 080030.
74 D. Fernandes, C. W. Raubach, P. L. G. Jardim, M. L. Moreira and S. S. Cava, *Ceram. Int.*, 2021, **47**, 10185–10188.
75 T. Li, G. Nam, K. Liu, J. H. Wang, B. Zhao, Y. Ding, L. Soule, M. Avdeev, Z. Luo and W. Zhang, *Energy Environ. Sci.*, 2022, **15**, 254–264.
76 J. Lee, D. A. Kitchaev, D. H. Kwon, C. W. Lee, J. K. Papp, Y. S. Liu, Z. Lun, R. J. Clement, T. Shi and B. D. McCloskey, *Nature*, 2018, **556**, 185–190.
77 S. L. Zhou, X. D. Han, X. Zhao and X. P. Jiang, *Symposium on Piezoelectricity, Acoustic Waves, and Device Applications*, 2015.
78 A. Ablat, M. Mamat, R. Wu, Y. Ghupur, T. Gholam, E. Muhemmed, J. Wang, H. Qian, R. Wu and K. Ibrahim, *Ceram. Int.*, 2016, **42**, 10624–10630.
79 A. Surendran, H. Enale, A. Thottungal, A. Sarapulova, M. Knapp, S. T. Nishanthi, D. Dixon and A. Bhaskar, *ACS Appl. Mater. Interfaces*, 2022, **14**, 7856–7868.
80 M. Pooladi, I. Sharifi and M. Behzadipour, *Ceram. Int.*, 2020, **46**, 18453–18463.
81 N. Meng, W. Liu, R. Jiang, Y. Zhang, S. Dunn, J. Wu and H. Yan, *Prog. Mater. Sci.*, 2023, **138**, 101161.
82 J. Ahmed, S. P., G. Vijaykumar, A. Jose, M. Raj and S. K. Mandal, *Chem. Sci.*, 2017, **8**, 7798–7806.